Combustion and Flame 287 (2026) 114917

Contents lists available at ScienceDirect

Combustion and Flame

journal homepage: www.sciencedirect.com/journal/combustion-and-flame

A physics-driven statistical mechanics framework for many-body thermodynamic and transport property computation

Xin Zhang, Hao Zhao *

School of Mechanics and Engineering Science, Peking University, Beijing 100871, China

ARTICLE INFO

Keywords:
Many-body interactions
Deep learning
Equation of state
Real-fluid modeling
Thermodynamic and transport properties

ABSTRACT

Many-body interactions play an important role in accurately modeling high-pressure thermodynamic and transport properties of real fluids. However, analytically resolving many-body interactions is computationally prohibitive. This work introduces a physics-driven statistical mechanics framework, which establishes a many-body virial (MB-Virial) equation of state (EoS) to compute real-fluid thermodynamic and transport properties. For predictions of compressibility, enthalpy, heat capacity, and viscosity, MB-Virial EoS consistently outperforms previous pairwise models. For polar species like H_2O and NH_3, it accurately captures the non-linear behaviors of the properties above within 15% errors between 1-600 atm, while pairwise models reach 270% errors. For long-chain alkanes such as n-C_5H_{12}, MB-Virial EoS maintains errors below 10% for heat capacity and viscosity predictions, whereas pairwise models often diverge beyond 50 atm. By accelerating computations 10^4 times faster than quantum calculations while maintaining an accuracy of < 0.1 kJ/mol, the MB-Virial approach offers a universal framework for many-body thermodynamic and transport predictions with various deep potential (DP) models, enabling next-generation simulations of supercritical fluids.

Novelty and significance statement

This work introduces a physics-driven statistical mechanics framework, the MB-Virial EoS, to compute real-fluid thermodynamic and transport properties. In this framework, various deep potential models are used to compute virial coefficients of the MB-Virial EoS directly from statistical mechanics, enabling systematic corrections to thermodynamic and transport properties, including enthalpy, heat capacity, viscosity, and thermal conductivity, over a wide range of temperatures and pressures. By explicitly linking microscopic many-body interactions with macroscopic fluid behavior, the MB-Virial EoS provides a general physics-driven statistical mechanics framework for formulating real-fluid properties directly from underlying potential models.

1. Introduction

Accurate predictions of thermodynamic and transport properties of real fluids are essential across a wide range of scientific and engineering processes, including energy conversion, heat and mass transfer, environmental modeling, and aerospace propulsion [1–4]. In particular, the access to real-fluid properties with high accuracy remains challenging under high pressure and non-equilibrium scenarios such as rocket propulsion, high-pressure combustion engines, spacecraft reentry, petroleum extraction, s-CO_2 power cycles, etc. [5–8]. In these regimes, standard modeling assumptions, most notably the ideal-gas behavior, begin to break down. As pressure rises above 200–400 atm, particularly in supercritical or compressed-fluid states, traditional pairwise potential models [9–13] can produce errors as large as 200% in predicting viscosity, thermal conductivity, and heat capacity.

These predictive failures originate from the drastic reduction in intermolecular spacing at elevated pressures, which induces severe overlaps among electron clouds and gives rise to polarization coupling and anisotropic many-body interactions [14]. Unlike dilute systems, where interactions can often be approximated as pairwise-addictive and isotropic, dense fluids, particularly those containing polar species, long-chain hydrocarbons, or reactive radicals, exhibit pronounced anisotropy and cooperativity [15,16]. Such effects generate non-additive contributions to the potential energy surface (PES) that are fundamentally inaccessible to two-body models [17]. As a result, real fluids in these regimes display complex behaviors, including continuous phase transitions, nonlinear thermodynamic responses, and sharp gradients in transport properties that deviate markedly from classical EoS [18].

Traditional semi-empirical approaches rely heavily on experimental measurements to parameterize or fit equations of state, such as van der

* Corresponding author.
E-mail address: h.zhao@pku.edu.cn (H. Zhao).

https://doi.org/10.1016/j.combustflame.2026.114917
Received 17 January 2026; Received in revised form 3 March 2026; Accepted 3 March 2026
Available online 6 March 2026
0010-2180/© 2026 The Combustion Institute. Published by Elsevier Inc. All rights are reserved, including those for text and data mining, AI training, and similar technologies.

Table 1
List of symbols.

Symbol	Description	Units
E_x	Energy of system x	J
p	Pressure	Pa
V_m	Molar volume	m^3/mol
V	Volume	m^3
T	Temperature	K
R	Ideal gas constant	J/mol/K
N_A	Avogadro constant	/mol
k_B	Boltzmann constant	J/K
$B(T)$	Second virial coefficient	m^3/mol
$C(T)$	Third virial coefficient	m^6/mol^2
φ	Intermolecular potential	J
r	Intermolecular distance	m
Z	Compressibility factor	–
H_m	Molar enthalpy	J/mol
S_m	Molar entropy	J/mol/K
$C_{p,m}$	Molar heat capacity at constant pressure	J/mol/K
η	Viscosity coefficient	μPa s
D	Diffusivity coefficient	cm^2/s
λ	Thermal conductivity	W/m/K
b_0	gas volume constant ($b_0 = \frac{2}{3}\pi N_A \sigma^3$)	m^3/mol
σ	molecular diameter	m
ϵ	Potential well depth	J
y	Correction factor from the partial derivation of the equation of state	–

Waals (vdW) [19], Redlich–Kwong (RK) [20], Soave–Redlich–Kwong (SRK) [21], and Peng–Robinson (PR) [22] models. However, in extremely high-pressure environments where experimental data are scarce or unavailable, their predictive accuracy deteriorates sharply [23–26]. Alternatively, high-level quantum chemistry calculations or other first-principles methods are highly required for predicting these real-fluid properties. For example, Bai and Zhang [9–13] employed the Virial EoS with ab initio pairwise potentials, the Lennard-Jones (LJ) [27,28] and Boltzmann-weighted Full-dimensional (BWF) [12] models, which improved predictions up to 200–400 atm. Nevertheless, such models inherently neglect many explicit-body collisions, approximating higher-order contributions through pairwise potentials. Their performance thus deteriorates rapidly in dense or supercritical fluids above 400 atm, where anisotropic and cooperative molecular interactions dominate. There is an urgent need for accurate many-body potential models, which are essential for reliable property predictions across a broad pressure range.

Despite the progress in many-body model development [29–31], accurately describing many-body collisions remains challenging. On one hand, traditional many-body models typically rely on predefined analytical functions with only a few parameters, which limits their ability to represent the complex anisotropic and non-additive interactions in strongly coupled molecular systems. On the other hand, the potential parameters are often optimized for specific molecules, resulting in poor transferability and repeated reparameterization for new systems or thermodynamic conditions. These limitations become even more severe under extreme environments such as high pressures and supercritical states [32,33], where traditional analytical many-body potentials often fail to yield reliable energy surfaces and derived properties across diverse chemical systems.

Recent advances in deep learning PESs provide a promising route to overcome these limitations [34–38]. Deep potential models can be trained directly on high-level quantum chemistry data and accurately capture complex many-body interactions [39]. However, a general framework that systematically connects microscopic many-body interactions to macroscopic thermodynamic and transport properties remains lacking. Most existing deep learning approaches are purely data-driven for predicting thermophysical properties. They typically rely on machine learning or regression models that map molecular descriptors directly to thermodynamic or transport properties [40–42]. While these models can achieve rapid and accurate predictions within the scope of the training data, they often suffer from limited interpretability of molecular physics and poor extrapolation for untrained molecules in a broad range of pressures and temperatures. This gap underscores the urgent need for a robust and physics-driven approach that can translate microscopic many-body interactions into thermophysical properties with statistical physics insights.

To address these challenges, we develop a physics-driven statistical mechanics framework, MB-Virial EoS, which establishes a direct pathway from advanced deep potentials to real-fluid properties via virial coefficients. In this framework, molecular PESs are represented using a typical many-body deep potential model with an attention mechanism, which integrates a deep neural network architecture with an attention mechanism to resolve full-dimensional PESs and capture cooperative many-body effects. These PESs are then used to compute virial coefficients of the MB-Virial EoS directly from statistical mechanics, enabling systematic corrections to thermodynamic and transport properties, including enthalpy, heat capacity, viscosity, and thermal conductivity, over a wide range of temperatures and pressures. By explicitly linking microscopic many-body interactions with macroscopic fluid behavior, the MB-Virial EoS provides a general physics-driven framework for formulating real-fluid properties directly from underlying potential models.

2. Theory and methods

The MB-Virial EoS is depicted in Fig. 1. It integrates high-level quantum chemistry data, deep neural networks, and statistical mechanics to construct a physics-driven computational model for thermodynamic and transport properties. First, a high-fidelity dataset of many-body intermolecular interactions is generated from dispersion-corrected density functional theory (DFT-D4). Second, deep neural network models are trained on these datasets to learn two- and three-body interaction potentials. Next, the DP model and Mayer-sampling Monte Carlo (MSMC) integration are employed to compute the second and third virial coefficients, which are then used to correct thermodynamic and transport properties. The symbols and variables in this paper are summarized in Table 1.

2.1. Data preparation

The two-body interaction data (Eq. (1)) have been reported in our recent studies [12,13]. For the calculation of three-body interactions (Eq. (2)), we employed the ORCA (version 5.0.3) software package [43], which offers both extensive functionality and high computational efficiency. The quantum chemical calculations were conducted using the PWPB95/def2-QZVPP combination for small molecules and the BLYP/def2-QZVPP combination for larger molecules [44]. The DFT-D4 method was applied to incorporate dispersion corrections into the DFT calculations, thereby providing a more accurate description of many-body interactions [45]. All quantum calculations include basis set superposition error (BSSE) corrections [46], ensuring that monomer, dimer, and trimer energies are consistently computed within the full cluster basis. The PWPB95/def2-QZVPP combination with D4 dispersion provides near-chemical accuracy (~1 kJ/mol) for noncovalent interactions, and the basis set is sufficiently large to approach the dispersion limit.

$$E_{ij}^{(2)} = E_{ij} - E_i - E_j \tag{1}$$

$$\begin{aligned} E_{ijk}^{(3)} =& E_{ijk} - (E_i + E_j + E_k) \\ & - (E_{ij}^{(2)} + E_{ik}^{(2)} + E_{jk}^{(2)}) \end{aligned} \tag{2}$$

The sampling strategy for the PES was designed to capture both spatial configurations and molecular orientations. As illustrated in Fig. 2(a)

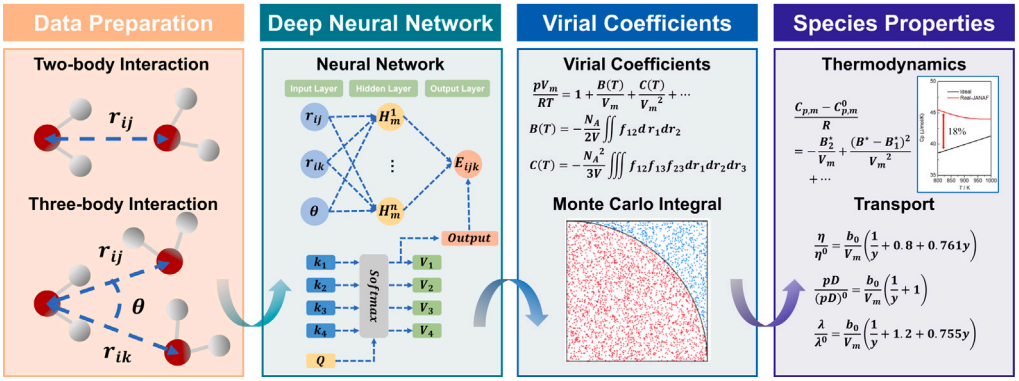

Fig. 1. The development and application process of the MB-Virial EoS.

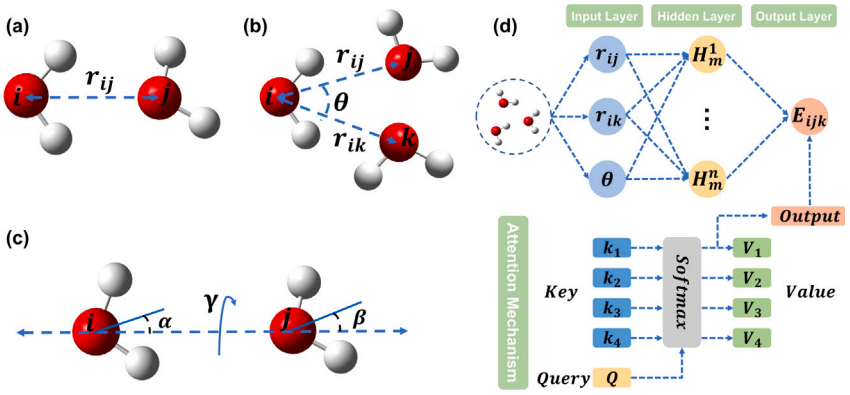

Fig. 2. (a) Two-body interaction defined by intermolecular distance r_{ij}, (b) three-body interaction defined by distances r_{ij}, r_{ik} and angle θ, (c) molecular orientation described by α, β, γ, and (d) the architecture of the deep potential with an attention mechanism.

and (b), two-body PESs were generated by varying the intermolecular distance r_{ij}, while three-body PESs were constructed by systematically adjusting the distances r_{ij}, r_{ik}, and the angle θ. Molecular orientations, depicted in Fig. 2(c), were described by three angles ($\alpha, \beta \in [0°, 180°], \gamma \in [0°, 360°]$). Using this comprehensive sampling strategy, we generated 7200 spatial configurations combined with 16 relative orientations, resulting in a full-dimensional PES dataset exceeding 10^6 points, covering nonpolar, polar, and long-chain molecular systems.

2.2. Deep neural network potential model

We develop a deep potential model to represent many-body intermolecular interactions, as shown in Fig. 2(d). The spatial configurations of molecular systems are described by intermolecular distances and angular coordinates, which are used as the input features of the neural networks. For each spatial configuration, the attention mechanism assigns weights to interaction energies associated with different molecular orientations, and the weighted PES is obtained through softmax normalization as the output reference. The neural networks are trained to learn the mapping from spatial configurations to the corresponding attention-weighted PES values. Model parameters are optimized by minimizing the mean squared error between the predicted interaction energies and the reference values obtained from quantum chemistry calculations. Training is performed using the Adam optimizer with k-fold cross-validation, and the training loss exhibits smooth convergence, as shown in Fig. 3.

2.3. Physical properties

We employ the Virial EoS, which is derived from statistical mechanics and provides a more accurate description of real-fluid behavior [47],

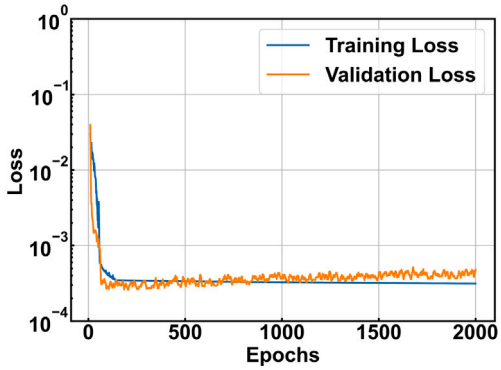

Fig. 3. Training loss curves of the deep potential model with an attention mechanism.

$$\frac{pV_m}{RT} = 1 + \frac{B(T)}{V_m} + \frac{C(T)}{V_m^2} \tag{3}$$

$$B(T) = -\frac{N_A}{2V} \int f_{12}\, d\mathbf{r}_1\, d\mathbf{r}_2 \tag{4}$$

$$C(T) = -\frac{N_A^2}{3V} \int \Big(f_{123} - f_{12} - f_{13} - f_{23} - f_{12}f_{13} - f_{12}f_{23} - f_{13}f_{23} \Big)\, d\mathbf{r}_1\, d\mathbf{r}_2\, d\mathbf{r}_3 \tag{5}$$

the Mayer function is defined as,

$$f = e^{-\varphi(r)/k_B T} - 1 \tag{6}$$

The form of $\varphi(r)$ is determined by the choice of potential model. For example, the LJ potential employs a simple isotropic two-body form, the BWF potential introduces the anisotropy through Boltzmann weighting, and the DP model in this work accounts for multi-body interactions based on neural networks. Substituting these different $\varphi(r)$ into the Mayer function (Eq. (6)) allows direct evaluation of $B(T)$ and $C(T)$ (Eqs. (4) and (5)), which in turn govern the Virial EoS and the calculation of thermodynamic and transport coefficients such as enthalpy, heat capacity, viscosity, thermal conductivity, and diffusivity [9].

Thus, by combining the Virial EoS with different potential models, we can systematically investigate how many-body effects influence thermophysical and transport properties across a wide range of pressures and temperatures. For deep potential models, we computed the second and third virial coefficients through MSMC integration [48]. The MSMC simulations were performed with a sampling distribution Π, where trial moves were accepted with a probability of $\min(1, \Pi_{\text{new}}/\Pi_{\text{old}})$,

$$B = B^{hs}\frac{\langle \tilde{B}/\Pi \rangle_{\Pi}}{\langle \tilde{B}^{hs}/\Pi \rangle_{\Pi}} \tag{7}$$

$\langle \dots \rangle_{\Pi}$ denotes the weighted average from MSMC simulations with the sampling distribution Π, and the superscript hs represents the hard-sphere fluid as the reference system. The MSMC evaluation of virial coefficients, using 10^7–10^8 sampling steps, lies well within the convergence range reported in the literature [48]. Comparison with direct formula calculations shows a relative deviation below 0.001%, indicating negligible numerical uncertainty. Replacing direct PWPB95-D4/def2-QZVPP calculations (10–30 min per configuration on 32 CPU cores) with the trained DP model (10^{-6}–10^{-4} s per evaluation on a single GPU) achieves an effective acceleration of 10^4–10^6 for practical virial coefficient computations.

3. Results and discussion

3.1. Potential energy surfaces

To evaluate the accuracy of the DP model in this work, we compared the predicted two- and three-body PESs by using the DP model against DFT-D4 reference data in Fig. 4. The training dataset comprised 200,000 dimer and 1,000,000 trimer configurations, spanning intermolecular separations from 2.0 to 7.0 Åand diverse intermolecular orientations. As to the two-body interactions in Fig. 4(a) and (b), the root-mean-square error (RMSE) for the PES prediction between the classical LJ model and DFT-D4 data remains 8.8015 kJ/mol, while the DP model exhibits excellent agreement within an error of 0.1280 kJ/mol, which is an order of magnitude smaller than the LJ model. Furthermore, the predicted three-body PES by using DP is within an error of 2.6642 kJ/mol against DFT-D4 data in Fig. 4(c) and (d), while the LJ model is not applicable to describe the many-body potential. The machine learning fitting error is much smaller than the typical three-body interaction energies (10^1-10^3 kJ/mol), making its fitting error negligible compared with $E^{(3)}_{ijk}$. Therefore, the DP model not only captures the two-body PES accurately, but is also successfully applied to describe the three-body topological PES by capturing both the steep repulsive wall at short separations and the attractive wells at intermediate distances.

3.2. Compressibility and thermodynamic properties

The compressibility factor and thermodynamic properties, such as specific enthalpy, specific entropy, and isobaric specific heat capacity, are computed using the pairwise potential models (Pairwise-LJ, Pairwise-BWF) and the MB-Virial EoS. They are subsequently compared against experimentally fitted data from the NIST library [49] across a broad pressure range in Fig. 5 (the entropy comparison is shown in Fig. S1, and the N_2 and H_2O data are provided in Fig. S4 of the Supplementary material).

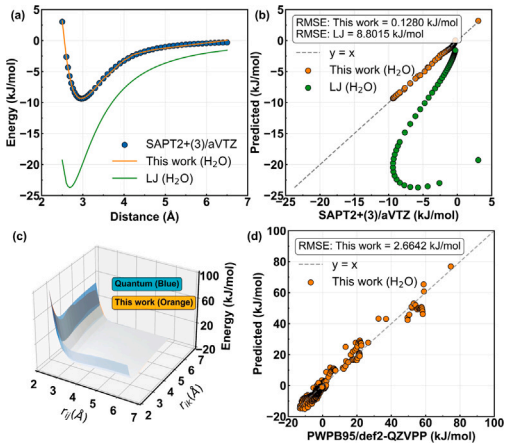

Fig. 4. Comparison of two-body and three-body potential energy surfaces: (a) two-body PES comparison between quantum calculations (SAPT2+(3)δMP2/aug-cc-pVTZ) and model predictions (the DP model in this work and LJ model); (b) RMSE scatter plot for two-body PES predictions; (c) three-body PES comparison between quantum calculations (PWPB95-D4/def2-QZVPP) and model predictions (the DP model in this work); (d) RMSE scatter plot for three-body PES predictions.

The comparison of the compressibility factor Z is depicted as a function of pressure in Fig. 5(a)–(c). At low pressures (< 50 atm), the compressibility factors of all molecules remain close to 1.0, consistent with the ideal-gas behavior. As pressure increases, enhanced intermolecular interactions and electron cloud overlap lead to deviations from ideality. For nonpolar molecules such as H_2, CH_4, and N_2, Z increases nearly linearly with pressure. All models, including LJ, BWF, and MB-Virial, accurately reproduce experimental trends up to 600 atm, with relative errors of less than 2%. The relative errors remain small and do not exhibit noticeable amplification with pressure for these nonpolar systems, indicating that two-body interactions dominate even at elevated pressures. In contrast, polar molecules, including H_2O, NH_3, and H_2S, display stronger and non-monotonic deviations. For H_2O and NH_3, LJ and BWF diverge above 400 atm, whereas MB-Virial maintains relative errors of 0.1%–6% between 1–600 atm. Notably, for LJ and BWF, the relative errors increase progressively with pressure, particularly beyond 300–400 atm, highlighting the growing importance of many-body interactions in dense polar fluids. For H_2S, Z decreases below 300 atm due to strong dipole–dipole attractions and weak hydrogen bonding, then increases as short-range repulsive forces become significant. The LJ model, constrained to isotropic two-body interactions, fails to capture its non-monotonic characteristics, with an error between 25%–30% exceeding 400 atm. Although the anisotropic BWF model reduces the relative errors to 15%, MB-Virial captures the non-monotonic behavior and agrees with the NIST data within 9% between 1–600 atm. The deviation of compressibility factor from ideality is further amplified in long-chain hydrocarbons, where multiple molecular segments interact simultaneously with neighboring molecules to form cooperative interaction networks. As shown in Fig. 5(c), long-chain hydrocarbons such as C_3H_8 and n-C_5H_{12} exhibit pronounced non-monotonic compressibility behavior. Both LJ and BWF fail to predict this real-fluid behavior, as the many-body interactions are not included in these models. However, MB-Virial accurately captures both the magnitude and the non-monotonic curvature of these hydrocarbons within errors of 18% over 1–600 atm.

The variation of specific enthalpy h with pressure is presented in Fig. 5(d)–(f). Unlike the compressibility factor, which primarily reflects volumetric response, enthalpy directly embodies the energetic

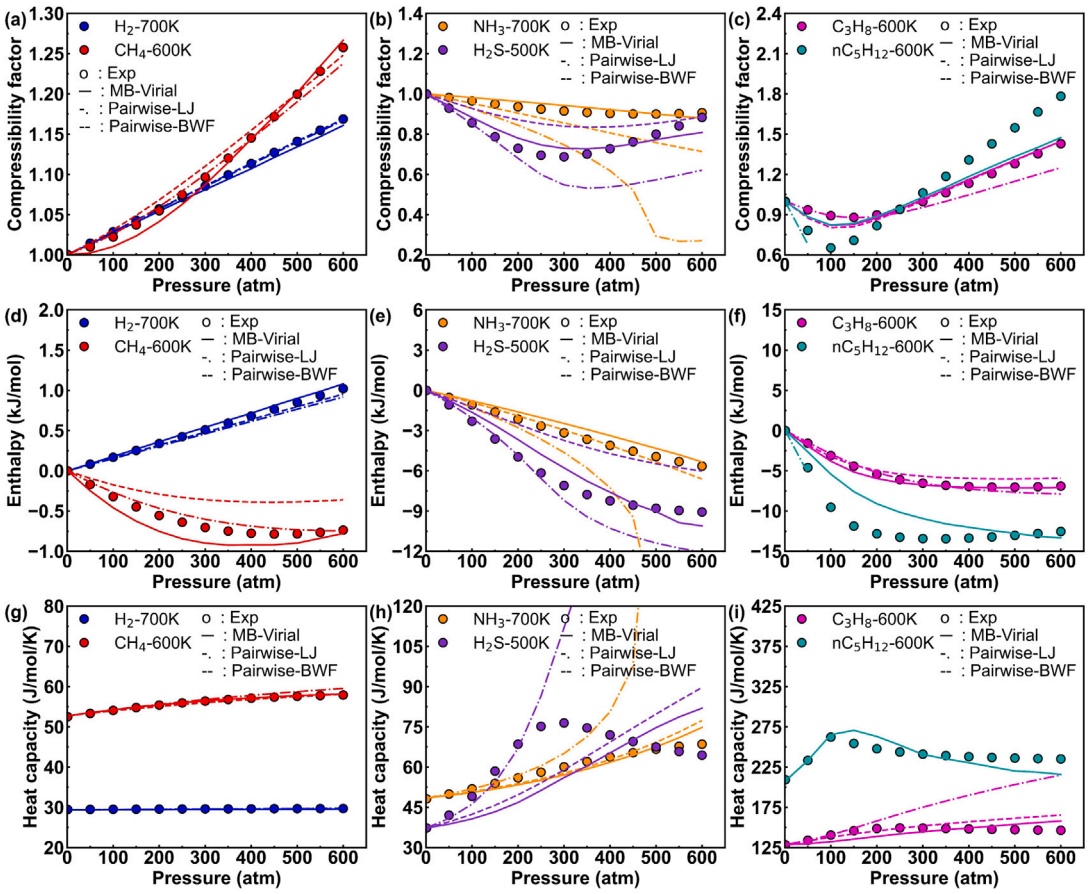

Fig. 5. The compressibility and thermodynamic properties of various models: (a) compressibility factor of nonpolar molecules; (b) compressibility factor of polar molecules; (c) compressibility factor of long-chain molecules; (d) specific enthalpy of nonpolar molecules; (e) specific enthalpy of polar molecules; (f) specific enthalpy of long-chain molecules; (g) isobaric specific heat capacity of nonpolar molecules; (h) isobaric specific heat capacity of polar molecules; (i) isobaric specific heat capacity of long-chain molecules.

balance between intermolecular attractions, repulsions, and PV work. For nonpolar gases such as H_2 and N_2, the enthalpy change is nearly linear with pressure, and LJ, BWF, and MB-Virial provide reliable predictions with deviations below 10% up to 600 atm. Both the MB-Virial and LJ models agree with the NIST enthalpy data for CH4 well between 1–600 atm, while the discrepancy of the BWF model gradually enlarges with pressure. In polar systems, the competition between dipole-driven attractions and short-range repulsions gives rise to pronounced non-linear behavior. As shown in Fig. S4 (d), for H_2O, the enthalpy decreases monotonically from 0 kJ/mol at 1 atm to −8.97 kJ/mol at 600 atm. The LJ model underpredicts the enthalpy with an error exceeding 40% at 400 atm, and the BWF model mitigates the discrepancy to 27% at 400 atm, while both models eventually diverge above 400 atm. In both LJ and BWF models, the magnitude of the error increases with pressure, reflecting the growing contribution of many-body polarization and cooperative interactions that are not fully captured by pairwise potentials. In contrast, MB-Virial reproduces the entire pressure-dependent curve with deviations below 35%. For NH_3, the LJ model diverges dramatically beyond 400 atm, producing errors over 200%, while the BWF and MB-Virial models maintain accuracy within a 28% error across the full pressure range. For H_2S, LJ and BWF underpredict and overpredict the enthalpy changes with errors exceeding 30%, while MB-Virial accurately captures the non-linear characteristics and maintains deviations below 12% above 400 atm. The predicted enthalpy for long-chain hydrocarbons such as C_3H_8 and n-C_5H_{12} is depicted in Fig. 5(f). MB-Virial exhibits a smaller error of 5% than that of 15% in LJ and BWF models for C_3H_8 in 1–600 atm. For n-C_5H_{12}, LJ and BWF start diverging above 50 atm, and their deviations progressively increase with pressure, whereas MB-Virial consistently follows the experimental trend and keeps an error below 45% even above 400 atm.

Fig. 5(g)–(i) present the pressure dependence of the isobaric specific heat capacity c_p. For nonpolar gases such as H_2, CH_4, and N_2, all these models predict c_p with errors below 3%. The relative errors exhibit minimal variation with pressure in nonpolar systems. For polar molecules such as H_2O and NH_3, the LJ and BWF models diverge beyond 400 atm, while MB-Virial maintains relative errors within 10% across the full pressure range. However, H_2S exhibits a distinctly non-monotonic c_p trend, increasing from 37.3 J/mol/K at 1 atm to a maximum of 76.5 J/mol/K at 300 atm, and subsequently decreasing to 64.4 J/mol/K at 600 atm. This behavior arises from the pressure-induced strengthening of intermolecular interactions as H_2S transitions from an ideal-gas-like to a non-ideal fluid state. Enhanced orientational correlations activate additional rotational and vibrational modes, increasing the heat capacity at low to moderate pressures. At higher pressures, molecular associations saturate, and orientational freedom is restricted, reducing compressibility and enthalpy sensitivity, which causes the heat capacity to decline. All three models fail to reproduce the non-monotonic behavior of H_2S from NIST data. The predicted c_p for long-chain hydrocarbons is shown in Fig. 5(i). LJ and BWF overestimate c_p of C_3H_8 and maintain 40% errors, whereas MB-Virial remains an error within 10%. For n-C_5H_{12}, the divergence of LJ and BWF shows a strong positive correlation with pressure due to neglect of cooperative interactions, whereas MB-Virial demonstrates improved robustness and captures the non-linear behavior of c_p with errors below 10%.

Therefore, it is seen from Fig. 5 that MB-Virial exhibits its priority for capturing the linear and non-linear change of compressibility, enthalpy, and heat capacity from low to ultra-high pressures in high accuracy for various nonpolar, polar, and long-chain molecules, while LJ and BWF often lose their accuracy at high pressures and are limited to predict the linear characteristics. In particular, the non-monotonic pressure dependence of H_2S and long-chain hydrocarbons reflects competing many-body effects. At intermediate pressures, enhanced orientational correlations strengthen effective attractions, reducing compressibility and altering the pressure derivative of enthalpy. At higher pressures, short-range steric (Pauli) repulsion and configurational entropy loss dominate, reversing the trends of thermodynamic derivatives and producing non-monotonic behavior. This crossover is naturally captured within the many-body virial framework through explicit three-body contributions that account for environment-dependent interactions. The superior performance of MB-Virial stems from its explicit treatment of many-body coupling, conformational flexibility, and vibrational mode confinement, which collectively govern thermodynamic responses under high-pressure conditions.

3.3. Transport properties

Viscosity offers a more reliable benchmark for validating transport models against pressure, as either experimental uncertainties remain high in thermal conductivity and mass diffusivity, or their experimental data is very rare at elevated pressures [50]. The predicted viscosity coefficients are shown in Fig. 6 as a function of pressure for different species, and the mass diffusivity and thermal conductivity coefficients are provided in Figs. S2 and S3 of the Supplementary material. As pressure increases, viscosity rises primarily because of the higher collisional frequency and enhanced momentum transfer between molecules. For small nonpolar molecules such as H_2, CH_4, and N_2, this effect is minor, and the LJ, BWF, and MB-Virial models remain accurate within 8%. In contrast, polar fluids exhibit a much steeper viscosity increase due to strong hydrogen bonding, dipole–dipole interactions, and orientation-dependent collisions, which promote more effective momentum exchange and thus higher resistance to shear flow. The LJ model severely diverges for predicting the viscosities of H_2O above 50 atm, NH_3 above 150 atm, and H_2S above 200 atm, and the deviation grows rapidly with pressure. Both the BWF and MB-Virial models capture the non-linear trends of the NH_3 and H_2O curves reasonably well across most pressure ranges, although BWF begins to diverge above 400 atm. For H_2S, both models exhibit maximum errors of approximately 30% over the range 1–600 atm. For long-chain hydrocarbons, the accuracy of these models strongly depends on the chain length. For C_3H_8, all three models provide reasonable predictions with errors of 1%–12% between 1–600 atm. However, the LJ and BWF models begin to diverge for n-C_5H_{12} as early as 50 atm, failing to compute higher-pressure viscosity coefficients. In contrast, the MB-Virial model successfully captures both the curve shape and values of viscosity within a 12% error even above 400 atm. It is seen that MB-Virial exhibits more accurate predictions for most nonpolar, polar, and long-chain molecules in this study than LJ and BWF, especially at high pressures, due to its consideration of many-body interactions. Overall, the error amplification with pressure is substantially mitigated in the MB-Virial framework, demonstrating its enhanced robustness in dense and strongly interacting fluid regimes.

3.4. Model analysis

We further summarize the contributions of the MB-Virial computation on each hydrodynamic and transport parameter for H_2O at 200 atm as an example in Fig. 7. It is seen that the MB-Virial method shows distinct impacts on these properties. The deviation in the isobaric heat capacity $C_{p,m}$ exceeds 20%, indicating strong sensitivity to high-pressure real-fluid effects, whereas the deviations in molar enthalpy H_m and entropy S_m remain within ±2%. In contrast, transport properties exhibit moderate and systematic deviations of approximately 5%–10%, reflecting a consistent correction under high-pressure conditions.

Our results uncover several key insights into the thermodynamic and transport behaviors of real fluids under a wide range of pressures, with direct implications for high-pressure combustion and process design. First, the emergence of non-monotonic pressure dependencies in key properties reflects a delicate competition between cooperative dipole–dipole attractions and short-range repulsions. For example, the compressibility factor of H_2S exhibits a non-monotonic trend, with deviations exceeding 15% when described by LJ or BWF, while MB-Virial reproduces the turnover with < 9% error. Similarly, CH_4 displays an enthalpy minimum of −0.786 kJ/mol near 450 atm, which is entirely missed by BWF but accurately captured by MB-Virial. Long-chain hydrocarbons such as n-C_5H_{12} also display strongly nonlinear heat capacity evolution, and only MB-Virial can reproduce this pressure dependence within 10% error, whereas pairwise potentials diverge rapidly beyond 50 atm. These results highlight that the non-monotonic response of real fluids is likely from the many-body effect, and that MB-Virial is capable of describing the collective rearrangements driving these trends.

Second, the consistently superior performance of MB-Virial across polar fluids and long-chain hydrocarbons demonstrates its ability to encode anisotropic many-body interactions, hydrogen bonding, and conformational flexibility, which are essential at high density. For instance, in NH_3, LJ enthalpy predictions diverge with errors above 200% at 600 atm, whereas MB-Virial maintains accuracy within 28%. For transport properties, MB-Virial accurately reproduces the steep viscosity rise of H_2S from 21.18 to 64.21 μPa s over 1–600 atm with < 30% deviation, compared with > 200% errors from the LJ model. These observations confirm that explicitly accounting for many-body physics, not just pairwise interactions, is crucial for quantitatively predicting thermodynamic and transport properties in dense fluids. Moreover, MB-Virial achieves the same or higher accuracy without parameter tuning against experimental data, thereby offering a transferable and physically grounded framework that is particularly valuable for radicals and short-lived intermediates where experimental measurements are scarce or unavailable.

Therefore, MB-Virial EoS is comprehensively applicable for nonpolar, polar, long-chain, and short-lived molecules and radicals in a broad range of temperatures and pressures. The MB-Virial framework is also adaptable for different DP models as well as traditional pairwise models. Incorporating advanced DP models further helps increase accuracy for thermophysical predictions in specific application scenarios. For example, prediction limitations exist in open-shell electronic structure calculations, cooperative dipole interactions, and weak hydrogen bonding for open-shell molecules like O_2 and certain strongly polar species like H_2S in this work, which can be mitigated by providing more accurate many-body models and higher-fidelity reference data.

4. Conclusion

In this work, we develop the MB-Virial EoS, a physics-driven statistical mechanics framework that systematically bridges microscopic many-body interactions and macroscopic thermodynamic and transport properties through statistical physics. The model consistently outperforms traditional pairwise models across diverse molecular systems, maintaining prediction errors within 15% for polar species like H_2O and NH_3 and below 45% for long-chain alkanes between 1–600 atm, whereas pairwise models exhibit errors up to 270% and often diverge beyond 50 atm. MB-Virial successfully captures complex non-monotonic pressure dependencies in thermodynamic properties, exhibiting the critical importance of explicitly accounting for many-body interactions, anisotropic effects, and conformational flexibility in dense fluid systems. The MB-Virial framework is adaptable for different DP models as well as traditional pairwise models. It enables

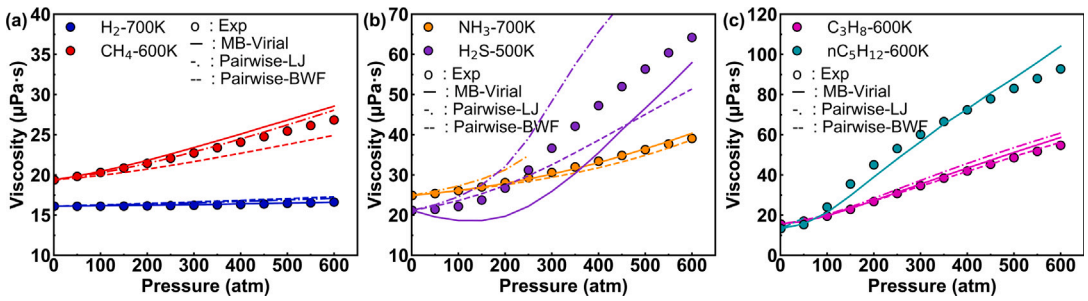

Fig. 6. The viscosity coefficients of various models: (a) nonpolar molecules; (b) polar molecules; (c) long-chain molecules.

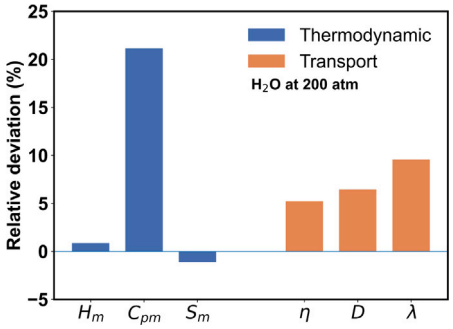

Fig. 7. Relative deviations of thermodynamic and transport properties of H_2O at 200 atm between the MB-Virial EoS and the ideal-gas models.

further high-accuracy predictivity for complex fluids in broader scenarios with advanced DP models. Overall, MB-Virial EoS establishes a new paradigm for real-fluid property prediction that bridges quantum-level accuracy with computational efficiency, opening new possibilities for next-generation simulations of supercritical fluids and high-pressure processes across energy conversion, aerospace propulsion, and environmental modeling applications. Future work will focus on extending and validating the MB-Virial framework for reactive and open-shell species, such as radicals, under extreme thermodynamic conditions to fully assess its transferability and predictive power.

CRediT authorship contribution statement

Xin Zhang: Writing – original draft, Validation, Software, Data curation, Conceptualization. **Hao Zhao:** Writing – review & editing, Supervision.

Declaration of competing interest

The authors declare that they have no known competing financial interests or personal relationships that could have appeared to influence the work reported in this paper.

Acknowledgments

This work was supported by the National Natural Science Foundation of China (No. 22350710788, No. 22361132538, No. 52576103, and No. W2533036).

Appendix A. Supplementary data

Supplementary material related to this article can be found online at https://doi.org/10.1016/j.combustflame.2026.114917.

References

[1] G. Lacaze, J.C. Oefelein, A non-premixed combustion model based on flame structure analysis at supercritical pressures, Combust. Flame 159 (2012) 2087–2103.
[2] X. Wang, H. Huo, U. Unnikrishnan, V. Yang, A systematic approach to high-fidelity modeling and efficient simulation of supercritical fluid mixing and combustion, Combust. Flame 195 (2018) 203–215.
[3] H. Zhao, J. Fu, F.M. Haas, Y. Ju, Effect of prompt dissociation of formyl radical on 1,3,5-trioxane and CH2O laminar flame speeds with CO2 dilution at elevated pressure, Combust. Flame 183 (2017) 253–260.
[4] H. Zhao, C. Yan, T. Zhang, G. Ma, M.J. Souza, C.-w. Zhou, Y. Ju, Studies of high-pressure n-butane oxidation with CO2 dilution up to 100 atm using a supercritical-pressure jet-stirred reactor, Proc. Combust. Inst. 38 (2021) 279–287.
[5] L. Jing, H.M. El-Houjeiri, J.-C. Monfort, J. Littlefield, A. Al-Qahtani, Y. Dixit, R.L. Speth, A.R. Brandt, M.S. Masnadi, H.L. MacLean, W. Peltier, D. Gordon, J.A. Bergerson, Understanding variability in petroleum jet fuel life cycle greenhouse gas emissions to inform aviation decarbonization, Nat. Commun. 13 (2022) 7853.
[6] H. Zhao, J. Fu, F.M. Haas, Y. Ju, Effect of prompt dissociation of formyl radical on 1,3,5-trioxane and CH2O laminar flame speeds with CO2 dilution at elevated pressure, "Combust. Flame" 183 (2017) 253–260.
[7] H. Zhao, C. Yan, T. Zhang, G. Ma, M.J. Souza, C.-w. Zhou, Y. Ju, Studies of high-pressure n-butane oxidation with CO2 dilution up to 100 atm using a supercritical-pressure jet-stirred reactor, "Proc. Combust. Inst." 38 (2021) 279–287.
[8] G. Li, Y. Lu, P. Glarborg, Development of a detailed kinetic model for hydrogen oxidation in supercritical H2O/CO2 mixtures, "Energy Fuels" 34 (2020) 15379–15388.
[9] J. Bai, P. Zhang, C.-W. Zhou, H. Zhao, Theoretical studies of real-fluid oxidation of hydrogen under supercritical conditions by using the virial equation of state, "Combust. Flame" 243 (2022) 111945.
[10] J. Bai, X. Zhang, C.-W. Zhou, P. Zhang, H. Zhao, Theoretical studies of supercritical real-fluid oxidations of diverse fuels by using the 3rd-order virial equation of state with nonlinear effects, "Combust. Flame" 270 (2024) 113728.
[11] J. Bai, X. Zhang, H. Zhao, Theoretical study of the real-fluid laminar flame propagation under supercritical conditions by using the virial equation of state and the enskog transport model, "Combust. Flame" 276 (2025) 114144.
[12] X. Zhang, J. Bai, B. Liu, T. Zhu, H. Zhao, Real-fluid transport property computations based on the Boltzmann-weighted full-dimensional potential model, "Appl. Energy Combust. Sci." 23 (2025) 100342.
[13] X. Zhang, J. Bai, H. Zhao, Studies of real-fluid supercritical simulation using the 3*rd* virial equation of state based on Boltzmann-weighted Full-dimensional potential, Combust. Flame 282 (2025) 114465.
[14] P. Zalden, L. Song, X. Wu, H. Huang, F. Ahr, O.D. Mücke, J. Reichert, M. Thorwart, P.K. Mishra, R. Welsch, R. Santra, F.X. Kärtner, C. Bressler, Molecular polarizability anisotropy of liquid water revealed by terahertz-induced transient orientation, Nat. Commun. 9 (2018) 2142.
[15] T. Dornheim, T. Döppner, P. Tolias, M.P. Böhme, L.B. Fletcher, T. Gawne, F.R. Graziani, D. Kraus, M.J. MacDonald, Z.A. Moldabekov, S. Schwalbe, D.O. Gericke, J. Vorberger, Unraveling electronic correlations in warm dense quantum plasmas, Nat. Commun. 16 (2025) 5103.
[16] C. Liu, R. Qi, Q. Wang, J.-P. Piquemal, P. Ren, Capturing Many-Body Interactions with Classical Dipole Induction Models, J. Chem. Theory Comput. 13 (2017) 2751–2761.
[17] J. Parker, S. Nagasamudram, C. Peterson, Y. Li, S. Soleimanikahnoj, S.A. Rice, N.F. Scherer, Symmetry breaking-induced N-body electrodynamic forces in optical matter systems, Nat. Commun. 16 (2025) 6294.
[18] E. Brini, C.J. Fennell, M. Fernandez-Serra, B. Hribar-Lee, M. Lukšič, K.A. Dill, How Water's Properties Are Encoded in Its Molecular Structure and Energies, Chem. Rev. 117 (2017) 12385–12414.
[19] R. Scott, P.V. Konynenburg, Static properties of solutions. Van der waals and related models for hydrocarbon mixtures, "Discuss. Faraday Soc." 49 (1970) 87.
[20] O. Redlich, J. Kwong, On the thermodynamics of solutions. V. An equation of state. Fugacities of gaseous solutions, "Chem. Rev." 44 (1949) 233–244.

[21] G. Soave, Equilibrium constants from a modified Redlich-Kwong equation of state, "Chem. Eng. Sci." 27 (1972) 1197–1203.
[22] D. Peng, D. Robinson, A new two-constant equation of state, "Ind. Eng. Chem. Fund." 15 (1976) 59–64.
[23] G. Kogekar, C. Karakaya, G.J. Liskovich, M.A. Oehlschlaeger, S.C. DeCaluwe, R.J. Kee, Impact of non-ideal behavior on ignition delay and chemical kinetics in high-pressure shock tube reactors, "Combust. Flame" 189 (2018) 1–11.
[24] W. Liang, W. Li, C.K. Law, Laminar flame propagation in supercritical hydrogen/air and methane/air mixtures, "Proc. Combust. Inst." 37 (2019) 1733–1739.
[25] G. Li, Y. Lu, P. Glarborg, Oxidation kinetics of methane and methane/methanol mixtures in supercritical water, "Ind. Eng. Chem. Res." 61 (2022) 3889–3899.
[26] H. Terashima, M. Koshi, Prediction of propagating flames under high-pressure conditions with real-fluid combustion modeling, "Proc. Combust. Inst." 39 (2023) 1823–1831.
[27] J.E. Lennard-Jones, On the determination of molecular fields. —II. From the equation of state of a gas, "Proc. R. Soc. Lond. A" 106 (1924) 463–477.
[28] W. Stockmayer, Second virial coefficients of polar gases, "J. Chem. Phys." 9 (1941) 398–402.
[29] D. Laghi, T. Macrì, A. Trombettoni, Excitations and stability of weakly interacting bose gases with multi-body interactions, "Phys. Rev. A" 96 (2017) 043605.
[30] D. Lee, A. Ozakin, A.G. Gray, Multibody multipole methods, "J. Comput. Phys." 231 (2012) 6827–6845.
[31] G.A. Cisneros, K.T. Wikfeldt, L. Ojamäe, J. Lu, Y. Xu, H. Torabifard, A.P. Bartók, G. Csányi, V. Molinero, F. Paesani, Modeling Molecular Interactions in Water: From Pairwise to Many-Body Potential Energy Functions, Chem. Rev. 116 (2016) 7501–7528.
[32] J.T. Willman, J.M. Gonzalez, K. Nguyen-Cong, S. Hamel, V. Lordi, I.I. Oleynik, Accuracy, transferability, and computational efficiency of interatomic potentials for simulations of carbon under extreme conditions, J. Chem. Phys. 161 (2024) 084709.
[33] D. Montes De Oca Zapiain, M.A. Wood, N. Lubbers, C.Z. Pereyra, A.P. Thompson, D. Perez, Training data selection for accuracy and transferability of interatomic potentials, Npj Comput. Mater. 8 (2022) 189.
[34] L. Zhang, J. Han, H. Wang, R. Car, W. E, Deep potential molecular dynamics: A scalable model with the accuracy of quantum mechanics, "Phys. Rev. Lett." 120 (2018) 143001.
[35] S. Batzner, A. Musaelian, L. Sun, M. Geiger, J.P. Mailoa, M. Kornbluth, N. Molinari, T.E. Smidt, B. Kozinsky, E(3)-equivariant graph neural networks for data-efficient and accurate interatomic potentials, "Nat. Commun." 13 (2022) 2453.
[36] C. Chen, S.P. Ong, A universal graph deep learning interatomic potential for the periodic table, Nat. Comput. Sci 2 (2022) 718–728.
[37] M. Kulichenko, K. Barros, N. Lubbers, Y.W. Li, R. Messerly, S. Tretiak, J.S. Smith, B. Nebgen, Uncertainty-driven dynamics for active learning of interatomic potentials, Nat. Comput. Sci. 3 (2023) 230–239.
[38] Y. Zhang, H. Wang, W. Chen, J. Zeng, L. Zhang, H. Wang, W. E, DP-GEN: A concurrent learning platform for the generation of reliable deep learning based potential energy models, Comput. Phys. Comm. 253 (2020) 107206.
[39] J. Behler, Four generations of high-dimensional neural network potentials, "Chem. Rev." 121 (2021) 10037–10072.
[40] S. Duffield, M. Aifer, G. Crooks, T. Ahle, P.J. Coles, Thermodynamic matrix exponentials and thermodynamic parallelism, Phys. Rev. Res. 7 (2025) 013147.
[41] D. Gokhale, P.K. Jain, X. Su, Viability of low solar efficiency materials for photoelectrochemical separations via thermodynamic modeling, Nat. Commun. 16 (2025) 7284.
[42] D. Melanson, M. Abu Khater, M. Aifer, K. Donatella, M. Hunter Gordon, T. Ahle, G. Crooks, A.J. Martinez, F. Sbahi, P.J. Coles, Thermodynamic computing system for AI applications, Nat. Commun. 16 (2025) 3757.
[43] F. Neese, The ORCA program system, "WIREs Comput. Mol Sci" 2 (2012) 73–78.
[44] D.A. Wappett, L. Goerigk, Benchmarking density functional theory methods for metalloenzyme reactions: The introduction of the MME55 set, "J. Chem. Theory Comput." 19 (2023) 8365–8383.
[45] E. Caldeweyher, S. Ehlert, A. Hansen, H. Neugebauer, S. Spicher, C. Bannwarth, S. Grimme, A generally applicable atomic-charge dependent London dispersion correction, "J. Chem. Phys." 150 (2019) 154122.
[46] M. Gutowski, J. Van Lenthe, J. Verbeek, F. Van Duijneveldt, G. Chał asinski, The basis set superposition error in correlated electronic structure calculations, "Chem. Phys. Lett." 124 (1986) 370–375.
[47] J. Hirschfelder, C. Curtiss, R. Bird, Molecular Theory of Gases and Liquids, second ed., John Wiley and Sons, Inc., New York, NY, 1964.
[48] J.K. Singh, D.A. Kofke, Mayer sampling: Calculation of cluster integrals using free-energy perturbation methods, "Phys. Rev. Lett." 92 (2004) 220601.
[49] M. Chase, C. Davies, J. Downey, D. Frurip, R. McDonald, A. Syverud, NIST JANAF thermochemical tables, 1985, Version 1.0. https://webbook.nist.gov/chemistry/.
[50] N. Brown, L. Bastien, P. Price, Transport properties for combustion modeling, "Prog. Energy Combust. Sci." 37 (2011) 565–582.